

Foreground model recognition through Neural Networks for CMB B -mode observations

F. Farsian,^{*a,b,c*} N. Krachmalnicoff,^{*a,b,c*} C. Baccigalupi^{*a,b,c*}

^{*a*}Scuola Internazionale Superiore di Studi Avanzati (SISSA),
, Italy

^{*b*}Istituto Nazionale di Fisica Nucleare (INFN),
, Italy

^{*c*}Institute for Fundamental Physics of the Universe (IFPU),
, Italy

E-mail: farsian@sissa.it, nkrach@sissa.it, bacci@sissa.it

Abstract. In this work we present a Neural Network (NN) algorithm for the identification of the appropriate parametrization of diffuse polarized Galactic emissions in the context of Cosmic Microwave Background (CMB) B -mode multi-frequency observations. In particular, we have focused our analysis on low frequency foregrounds relevant for polarization observation: namely Galactic Synchrotron and Anomalous Microwave Emission (AME). We have implemented and tested our approach on a set of simulated maps corresponding to the frequency coverage and sensitivity represented by future satellite and low frequency ground based probes. The NN efficiency in recognizing the right parametrization of foreground emission in different sky regions reaches an accuracy of about 90%. We have compared this performance with the χ^2 information following parametric foreground estimation using multi-frequency fitting, and quantify the gain provided by a NN approach. Our results show the relevance of model recognition in CMB B -mode observations, and highlight the exploitation of dedicated procedures to this purpose.

¹Corresponding author.

Contents

1	Introduction	1
2	Foreground Parametrization and Simulations	3
2.1	Synchrotron Emission	3
2.2	Thermal Dust Emission	3
2.3	Anomalous Microwave Emission	4
2.4	Simulations	4
3	Neural Network architecture	6
3.1	NN for binary classification	7
3.2	NN for multi-classification	7
4	Results	8
4.1	Foreground model recognition via binary classifications	8
4.1.1	Synchrotron curvature	8
4.1.2	Synchrotron and AME	10
4.2	Multi-model classification	10
4.3	Classification in presence of noise	12
5	Comparison with the χ^2 information	14
6	Conclusion	16

1 Introduction

The Cosmic Microwave Background (CMB) and its polarization are one of the most important probes for Cosmology. The CMB is partially linearly polarized due to Thomson scattering at the epoch of recombination [1], and its polarization state can be described by the standard Stokes parameter, Q and U . The CMB polarization pattern can be also decomposed into an alternative base, the B and E -modes [2, 3], with odd and even behavior with respect to parity transformation, respectively. Primordial Gravitational Waves (GWs) produced by Inflation era in early Universe are sources of the CMB B -mode anisotropies, and represent the main observational target of ongoing and future CMB probes [see 4, and references therein]. A second relevant and non-primordial source of B -mode anisotropies is represented by the gravitational lensing of CMB photons by forming large scale structure (LSS). The CMB lensing signal is fundamental for investigating the dark cosmological components of the universe through LSS. The GW contribution to B -modes, parametrized by its amplitude relative to primordial scalar perturbations, the tensor-to-scalar ratio r , cause anisotropies at the degree and super-degree scale. The lensing signal dominates the B -mode spectrum at the arcminute scale.

Given the almost perfect Gaussianity of the CMB signal, its anisotropies are fully characterized in terms of angular power spectra, which have been observed with great accuracy on the full sky, for the total intensity (T) and E -mode polarization, by the Wilkinson Microwave Anisotropy Probe (WMAP) [5] and Planck [6] satellites. An intense and global effort

is currently ongoing towards the measurement of the B -mode polarization. Lensing B -modes have been detected, for the first time by the South Pole Telescope (SPTpol) [SPTpol, see 7, and references therein] through cross-correlation, and by POLARBEAR [8] through direct measurement. Moreover, they have been observed by the Planck satellite [9], the Background Imaging of Cosmic Extragalactic Polarization 2 (BICEP2) [10], the Atacama Cosmology Telescope (ACT) [11]. On the other hand and so far, only upper limits exist for the amplitude of the cosmological GWs, corresponding to $r < 0.06$ (at 95% confidence level) [12].

In the last years it has become clear that one of the greatest challenge for the detection of primordial B -modes is represented by the control and removal of the diffuse emission from our own Galaxy. As a matter of fact, Galactic polarized radiation has an amplitude larger than the cosmological signal on the degree and super-degree scales, at all frequencies and in all sky regions [see 13–15, and references therein]. In order to face this challenge and be able to extract a clean cosmological signal, future CMB probes are characterized by a multi-frequency coverage, with very high sensitivity detectors in all the frequency channels. Along this line, several observatories are currently being built, in particular, The Simons Array [SA, see 16] is being deployed, and the Simons Observatory [SO, see 17] will start operations in the early years of this decade. On the longer term, the Stage-IV network of ground-based observatories [CMB-S4, see 18], along with the Light satellite for the study of B -mode polarization and Inflation from cosmic microwave background Radiation Detection (LiteBIRD)[19], are designed to reach an accuracy, after foreground subtraction, corresponding to the capability of detecting a B -mode signal with r as low as 10^{-3} with high confidence level.

In the data analysis layer dedicated to the removal of diffuse foregrounds from the CMB signal, usually called component separation, the multi-frequency observations are analyzed and combined in order to reconstructed clean maps of the different sky components. In particular, typical methods for component separation are based on parametric fitting of the multi-frequency maps, where the parameters of the problem are those related to the amplitude and frequency scaling of the different foreground components. Therefore, a crucial aspect, which constitutes the focus of the present work, is represented by the need of having an accurate knowledge of how to parametrize the foreground emissions and how this parametrization might vary across the sky. A wrong or inaccurate modeling of Galactic radiation could indeed lead to high residuals in the final CMB maps, preventing the measurement of the faint B -mode cosmological signal.

This issue can be thought as a model recognition problem, which represents one of the most important applications of Artificial Intelligence (AI). Neural Networks (NNs) and Machine Learning (ML) in general, as a subset of AI, can be very useful in Cosmology and specifically in CMB field. In particular, NNs are non-linear mathematical tools with many parameters which are able to model different problems with high complexity. For this reason they are widely used in science. In the recent years, an effort to apply this tool in Cosmology is ongoing, as several papers explicitly show, with applications ranging from estimating cosmological parameters from dark matter [20], to real-time multimessenger astronomy for the detection of the gravitational wave signal from black hole merger [21] and weak lensing reconstruction via deep learning [22]. Recent applications, specific to CMB, are: foreground removal from CMB temperature maps using an MLP neural network [23], a convolutional neural networks for cosmic string detection in CMB temperature map [24], lensing reconstruction [25] and convolutional NNs on the HEALPix sphere [26].

In this paper, we present a new NN application concerning the classification of the appropriate foreground model across the sky, identifying which physical parametrization describes

better a multi-frequency dataset in the different sky regions. This classification has to be seen as a pre-processing to the component separation phase, to instruct the latter with the proper functions to be exploited for the fitting. We have focused the analysis on the diffuse Galactic emissions which dominate the low frequency range, i.e. 70 GHz or less, in CMB B -mode observations, taking into account, as a case study, the specifications of the LiteBIRD satellite [19] and the low frequencies instrument of the Q and U Joint Observatory in Tenerife [QUIJOTE 27], in terms of frequency coverage, angular resolution, and sensitivity. Our aim is to study if a pre-processing model recognition phase is possible, and with which efficiency and accuracy.

This paper is organized as follows: in Section 2 we review the spectral behavior and parametric models of diffuse Galactic foregrounds which are important for polarization. In Section 3 we describe how NNs work, emphasizing the aspects which are particularly relevant for this work, and define the architecture we have adopted. In Section 4 we study the performance and accuracy of the NN in distinguishing different foreground models distributed differently across the sky. In Section 5 we compare the information provided by the NN with the one from a standard approach. Finally, in Section 6 we bring up the discussion and conclusions.

2 Foreground Parametrization and Simulations

The main physical mechanisms which are responsible for the emission of linearly polarized light in our own Galaxy are represented by Galactic synchrotron and thermal dust. As described later, in our analysis we have also taken into account a third possible source of Galactic polarized radiation, generated by the spin of dust grains, known as Anomalous Microwave Emission (AME), see [13] and reference therein. In the following Sections we summarize the main characteristics of these emissions, and how we have simulated them in our work.

2.1 Synchrotron Emission

The synchrotron radiation is generated by cosmic-ray electrons accelerating in the Galactic magnetic field. It dominates over the CMB at frequencies ≤ 70 GHz and it possesses a steep Spectral Energy Distribution (SED) due to the corresponding energy distribution of electrons. At first order synchrotron SED can be parametrized as a simple power law in brightness temperature. Nonetheless, the energy distribution of electrons may be responsible for a curvature in the SED, which departs from a pure power law. The general model for synchrotron emission can be written as:

$$T(\hat{n}, \nu) = A_s(\hat{n}) \left(\frac{\nu}{\nu_0} \right)^{\beta_s(\hat{n}) + C(\hat{n}) \log(\nu/\nu_0)}, \quad (2.1)$$

where A_s is synchrotron amplitude at the pivot frequency ν_0 , β_s is the synchrotron spectral index, and C parametrizes SED curvature. In general, all quantities are functions of the sky direction \hat{n} . The synchrotron spectral index has a typical value $\beta_s \approx -3$, with variation in the sky at the level of few percent on the degree scale.[15].

2.2 Thermal Dust Emission

Thermal dust emission comes from interstellar dust grains which tend to align perpendicularly to the Galactic magnetic field, therefore emitting partially linear polarized radiation. Dust

grains are heated by starlight, and possess a modified black body SED, known as grey body, with a temperature T_d of about 20 K. The SED is also described by the emissivity β_d , which determines the deviation from a pure black body, and has a value of about 1.6. Thermal dust emission dominates the polarized sky radiation at frequencies ≥ 70 GHz. The analytic form of the brightness emission of the SED can be written as:

$$T(\hat{n}, \nu) = A_d(\hat{n}) \left(\frac{\nu}{\nu_0} \right)^{\beta_d(\hat{n})} B(\nu, T_d(\hat{n})), \quad (2.2)$$

where A_d defines the dust amplitude varying across the sky at the pivot frequency ν_0 , and B represents the standard black body spectrum at the temperature T_d and frequency ν .

2.3 Anomalous Microwave Emission

In total intensity, the AME has been observed by the QUIJOTE telescope and the Planck experiment in the frequency range ≈ 10 -60 GHz [28]. A possible explanation of this emission is represented by the spinning of the dust grains, which rotate at GHz frequencies and emit electric dipole radiation if they have an electric dipole moment [29], or magnetized dust grains and free-floating ferromagnetic material [30]. The AME SED is expected to exhibit a bell shape form, characterized by a peak at around 30 GHz. If AME is polarized, its polarization fraction must be very small, at the level of percent [28]. The QUIJOTE [31], for example, have constrain the AME polarization to be $< 2.8\%$ with 95% confidence level.

In this work, we adopt the standard model of the AME, constituting of simulated polarized maps with thermal dust polarization angles and nominal AME intensity with a global 2% polarization fraction, within the limits observed by WMAP, Planck and QUIJOTE. The parametrization of this model for AME SED is based on Ali-Haimoud et al. [32] paper. The spinning dust grains with an angular velocity ω of electric dipole moment μ can radiate as follow:

$$P = \frac{2}{3} \frac{\mu_{\perp}^2 \omega^4}{c^3}, \quad (2.3)$$

where P is the radiation power and μ_{\perp} is the perpendicular component of μ to ω . This power is emitted at the frequency $\nu = \omega/2\pi$. The emissivity of electric dipole radiation per Hydrogen (H) atom can be calculated through:

$$\frac{j_{\nu}}{n_H} = \frac{1}{d\pi} \int_{a_{min}}^{a_{max}} da \frac{1}{n_H} \frac{dn_{gr}}{da} 4\pi\omega^2 f_a(\omega) 2\pi \frac{2}{3} \frac{\mu_{a\perp}^2 \omega^4}{c^3} \quad (2.4)$$

where $\omega = 2\pi\nu$. The term $\frac{1}{n_H} \frac{dn_{gr}}{da}$ determines the grain size distribution function which gives the number of dust grains per unit size per H atom, $\mu(a)$ is the electric dipole moments as a function of grain size and $f_a(\omega)$ is the angular velocity distribution function which depends upon the grain radius and environmental condition. This function is calculated for a cold neutral medium in the simulations we adopt.

2.4 Simulations

In this section we describe the set up adopted to simulate the sky maps used to train and test our NN. As anticipated, we have focused our attention on low frequency foregrounds, and we have considered the frequency channels covered by the future LiteBIRD satellite [19] plus the two lowest frequency bands of the QUIJOTE telescope[27]. The corresponding

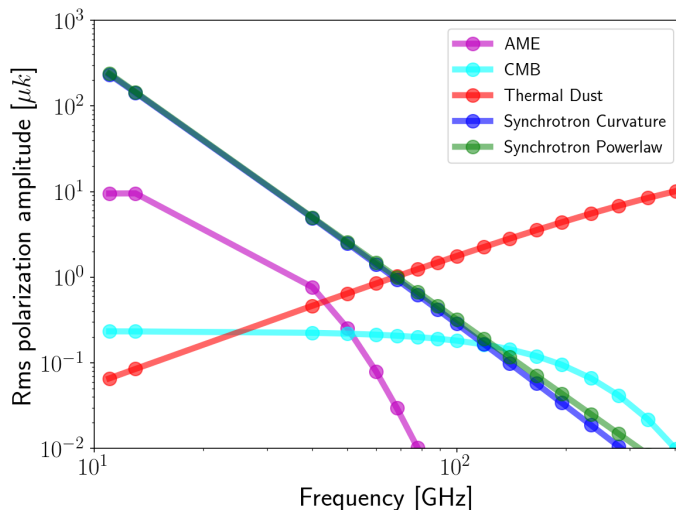


Figure 1. Total Polarized intensity rms amplitude as a function of frequency and different foreground component models which is used in our simulation. The plot refers to the full sky at the resolution of about 10 degrees, and brightness temperature units are considered.

frequencies, together with sensitivities and angular resolutions for all the considered channels are summarized in Table 1.

The sky emissions we have included in our simulations are: the CMB radiation, contaminated by the Galactic synchrotron, thermal dust and possibly polarized AME. All the components including the sky modeling of the Galactic emissions have been generated through the `Python Sky Model (PySM)`¹ publicly available package which generates the full-sky simulation in intensity and polarization.[33].

In particular, the CMB maps are generated as random Gaussian realizations of the Planck best fit Λ Cold Dark Matter (Λ CDM) power spectrum [6]. For the Galactic dust emission we have used the PySM template, rescaled as a modified blackbody, as in Equation (2.2), with constant spectral index $(\beta_d, T_d) = (1.54, 20K)$. For Synchrotron, we have considered two different models. In the first one, the template is extrapolated in frequency with a simple power law model. The spectral index is spatially varying, considering a Gaussian distribution with mean value $\beta_s = -3$ and standard deviation equal to 0.2. In the second case, a curvature is included in the synchrotron SED, with a constant value of $C = -0.052$, as indicated by Kogut [34] with 23 GHz as the pivot frequency; this setup is also compatible with the recent analysis by Krachmalnicoff et al. [15]. Finally, as explained in the following Sections, we have also included, in some specific cases, the AME polarized signal, assumed to have a 2% polarization fraction. The noise is simulated uniformly in the sky, through Gaussian realizations with standard deviations given by the parameters listed in Table 1. As an illustration of the relative relevance of the various components, in Figure 1 we plot the rms of total polarized intensity of the various sky emissions considered in this paper. To plot Figure 1 we took into account full-sky simulations in brightness temperature units at $N_{side} = 16$ for all the frequencies of LiteBIRD satellite and the two lowest frequency bands of the QUIJOTE telescope, computing rms of Q and U maps separately and obtaining the total polarization through $P = \sqrt{Q^2 + U^2}$.

¹https://github.com/bthorne93/PySM_public

Experiment	Frequency [GHz]	Sensitivity [μ K-arcmin]	FWHM [arcmin]
Quijote	11.0	840.0	55.2
	13.0	840.0	55.2
LiteBIRD	40.0	36.1	69.2
	50.0	19.6	56.9
	60.0	20.2	49.0
	68.0	11.3	40.8
	78.0	10.3	36.1
	89.0	8.4	32.3
	100.0	7.0	27.7
	119.0	5.8	23.7
	140.0	4.7	20.7
	166.0	7.0	24.2
	195.0	5.8	21.7
	235.0	8.0	19.6
	280.0	9.1	13.2
	337.0	11.4	11.2
402.0	19.6	9.7	

Table 1. Frequencies and instrumental specifications for QUIJOTE and LiteBIRD. The values are consistent with recent studies, [35], [4], respectively.

3 Neural Network architecture

In this work we have used NNs as a tool to recognize the optimal parametrization of Galactic foreground in the sky. Generally speaking NNs are algorithms that recognize underlying relationships in a set of data. Given a function f that maps an input x into an output y , the goal of a NN is to find the best approximation f^* of f . In order to do that, the NN recursively applies non-linear functions to linear combinations of the input elements. In this way, the function f^* depends on several parameters θ (the coefficient of the linear combinations) which need to be optimized in order to get $f^*(\theta) \approx f$. This is done through a *training set*, i.e. a set of data for which the real output $y = f(x)$ is known: by computing the NN output \tilde{y} for the elements of the training set, and by minimizing the distance between y and \tilde{y} , the best value for the NN parameters θ is found. The optimization is done numerically, usually with a stochastic gradient descent method, and the function that encodes the distance between y and \tilde{y} is called *loss function* [36].

There exist several different NN architectures. In this work we make use of a so called *fully connected* ones. The basic structure of this NN is a *neuron*. Neurons are organized in layers and in each of them a linear combination of all the elements of the previous layer is computed. Linear combinations are activated through a non-linear *activation function*, and the outputs of this operation become the inputs of the following layer. In the *input layer*, each neuron take the value of the elements of the input x , while in the output layer the neurons take the values of the elements of \tilde{y} . All the layers between the output and input ones are called *hidden layers*.

In our problem, the input of the NN are vectors of dimension 2×17 . Each element of this vector represents the amplitude of the sky signal in a given pixel and at the different

considered frequencies (17 in total) for the one of the two Stokes parameter Q and U . As the purpose of this work is to solve a classification problem (assigning the each pixel in the sky to a specific foreground model) the output of the NN is a vector where each element gives the probability that the input pixel belong to any of the considered classes (models); the dimension of the output vector depends on how many possible sky models are considered, as explained in the following sections.

As said, the value of the parameters θ that results in the best approximation of f are found through an iterative process, where the NN runs on the training set elements. The values of the θ parameters are updated at each *epoch*. Given the very large number of parameters that a NN needs to optimize, overfitting may occur; in this case, the NN approximates well the function f on the training set but it is unable to generalize to other set of data. To avoid this, a typical approach is to introduce the so called *dropout*, i.e. a mechanism for which, in each epoch, some of the neurons of the NN are randomly switched off. This prevents the NN to rely on any specific parameter and allow to mitigate overfitting.

We have built the NNs in the *Keras*² environment, which is a *Python* library, with *Tensorflow*³ backend. We have considered two NN architectures, which correspond to the problems we want to analyze, as described in the following.

3.1 NN for binary classification

In this first considered case, we have trained the NN to perform a binary classification, meaning that its goal is to assign to any pixel in the sky one out of two possible foreground models. As we specified above, the NN input layer has dimensionality 2×17 , then 3 hidden layers are present, including 68, 34 and 17 neurons each, with *tanh* as activation function. In order to prevent overfitting, a dropout layer with dropout rate = 0.5 is applied on the layer with the most numerous neurons. Since we are in the case of binary classification, the output layer, activated with a *sigmoid* function, has dimensionality 1, corresponding to the probability of the input to belong to the first class. Figure 2 shows the schematic architecture of our binary classifier. The loss function is defined as a binary-crossentropy function: $L = (z \log(p) + (1 - z) \log(1 - p))$, where p is the predicted probability for each input to belong to the specific class and z is the binary indicator associated to the two classes (0 or 1). We have used *Adadelta* optimizer with learning rate = 1.0 which is implemented in *Keras*.

3.2 NN for multi-classification

As explained in the following sections, we have also considered a case where the NN has to distinguish among 4 different sky models. Due to the enhanced complexity with respect to the binary classification, we increase the number of layers and neurons accordingly. In particular in this case the NN has 5 hidden layers with 272, 136, 68, 34 and 17 neurons, with *tanh* activation function. As before a dropout layer with dropout rate = 0.5 is applied on the first hidden layer with 272 neurons. The output layer is a multi-classification, with *softmax* function as activation. A Sparse-Categorical-Cross-entropy is chosen as loss function, corresponding to $L = - \sum_{c=1}^M z_{o,c} \log(p_{o,c})$, where M is the number of categories for classification and p is predicted probability for specific observation (o) of category c and z represents the correct class indicator for that observation (o). The same optimizer as binary classification is considered.

²<https://keras.io>

³<https://www.tensorflow.org>

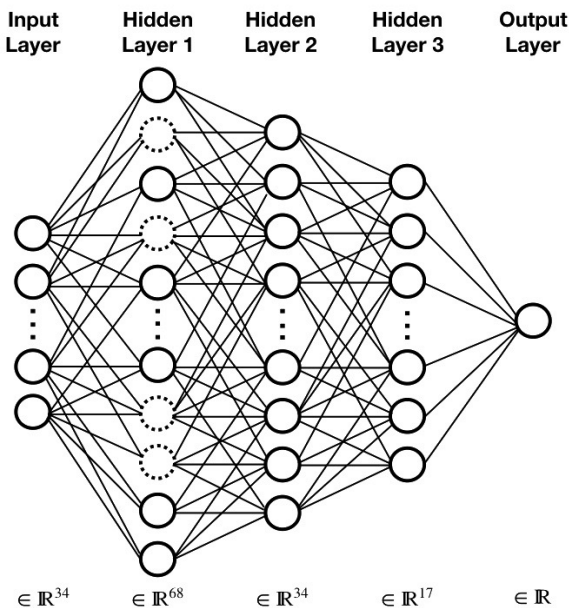


Figure 2. Schematic NN architecture used for binary classification: each circle represents a neuron, and the dashed circles indicate the application of dropout to a layer.

4 Results

We now discuss the results of model recognition for low frequency foregrounds via NNs, both in binary and multi-model classification. The analysis is entirely based on simulated polarization maps, where the signal information is given via the Q and U Stokes parameters. We study noisy and noiseless simulated maps at LiteBIRD and QUIJOTE frequencies, as anticipated. In the following Sections we describe the results for the different considered test cases.

4.1 Foreground model recognition via binary classifications

We first use the binary classifier described in Section 3.1 to distinguish between two different foreground models. In particular, in the first case we train the NN to understand whether low frequency data are fitted better by a synchrotron model which does or does not include curvature of the spectral index (see Equation 2.1). Next, we focus on the case in which the synchrotron emission is described by a pure power law and the NN is trained to recognize the presence of polarized AME.

4.1.1 Synchrotron curvature

In this first case we have trained the NN with four sets of simulated maps. We recall that each set of maps consists in 34 sky maps: 17 frequencies and Stokes Q and U emissions. In each set we have included the emission coming from CMB, polarized thermal dust and synchrotron. In the two first sets of maps, synchrotron emission is scaled in frequency with a pure power law, while in the others a curvature is added to the spectral index. We have considered a different random realization of the CMB emission for the each set of maps, as well as a different realization of the synchrotron spectral index spatial variation, which is taken from a Gaussian distribution with mean -3 and standard deviation 0.2. The synchrotron curvature

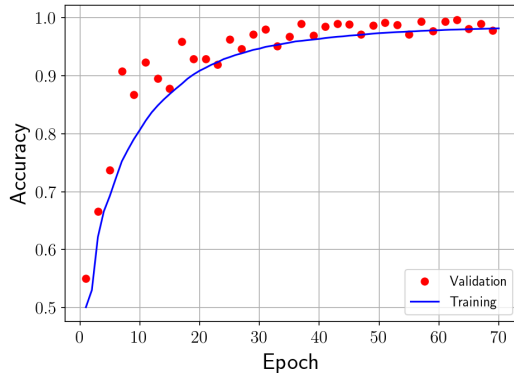


Figure 3. NN accuracy across training with respect to epochs for binary classification between synchrotron with and without curvature, in the noiseless case.

in the two sets of maps is constant, with a value $C = -0.052$, and 23 GHz as the pivot frequency. All the maps have been simulated at $N_{side} = 1024$, this means that in total we have about 5×10^7 vectors to be used for training. Among these, we have randomly selected 20% of them, which are not used for optimize the NN weights, but as validation set, as it is typically done for validate the performance of a NN. Since we have considered all the pixels in the sky maps, and given the high level of non-stationarity of the Galactic signals, the vectors in the training set cover a huge dynamic range, of about four orders of magnitude. As an usual step for data preparation to train the NN, we normalized the input vectors as following procedure, calculating minimum and maximum value for each input vector, subtracting the minimum value to the vector elements and dividing by difference between maximum and minimum value. In order to further generalize the training set, we have shifted the amplitude of each Galactic component in Q and U by multiplication of random value drawn from a Gaussian distribution with standard deviation equal to 30% of the amplitude of the signal in each pixel. We applied this shift in the template maps for Dust and Synchrotron components in PySM package, then the multi-frequency maps are scaled with proper relation from these modulated template maps.

The training history is shown in Figure 3: the accuracy (percentage of pixel correctly classified) of the NN on the training set is about 99% after 70 epochs. The red dots represent the accuracy on validation set, which is increasing with the iterations reaching a similar value of $\sim 98\%$.

Once the NN is trained, we can apply it to the test set. In particular, we have built test maps, by making use of the PySM library, that include CMB, synchrotron and thermal dust, similarly to the training set. Maps of the test set have been generated at $N_{side} = 16$; in some regions the synchrotron as been rescaled with a simple power law, in others we have included a running of the spectral index in the SED. An example of a test set map is reported in Figure 4: in the pixels belonging to the red regions the synchrotron SED is a pure power law, while in the blue region a curvature is added. The color scales report the output of the NN, i.e. the probability that each pixel belong to the associated category. Pixels with lighter colors are those where the NN have assigned the wrong model. For clarity, in the right panel of Figure 4, we show, in white, those pixels where the NN has done a wrong prediction. The reached accuracy is about 98% with no significant correlation between the morphology of the

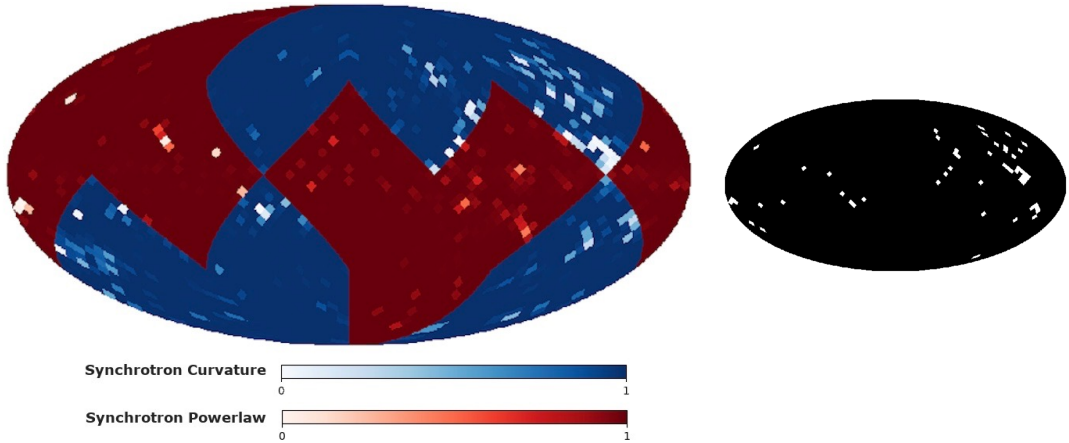


Figure 4. Left panel: NN prediction on test set for the binary classification for Galactic synchrotron with (blue regions) and without curvature (red regions) in the ideal case of noiseless maps. The color bar shows the NN probability assigned to the corresponding model across the sky. White pixels are those where the wrong model is assigned. Right panel: For clarity, correct (black) and wrong (white) pixels are also shown with a binary color scale.

sky signal and the position of wrong assignments.

4.1.2 Synchrotron and AME

We have used the same NN architecture for binary classification with the goal to identify those pixels where AME polarized radiation is present in the sky. The two models considered in this case correspond therefore to Galactic synchrotron with a pure power law SED, or synchrotron plus polarized AME component.

We have followed a procedure analogue to the one presented in the previous Section. As before the training set consists of four sets of maps, two first sets with CMB, synchrotron and thermal dust emission, the others with also polarized AME. Total number of pixels in the training set is more than 1.7×10^9 . Results are presented in 5, where regions where AME is present are shown in green. In the ideal noiseless case the NN is able to correctly classify the foreground model in about 97% of the cases.

4.2 Multi-model classification

We now extend the study performed so far and consider a more complex case in which the NN is trained to classify four different SEDs in the simulated sky. In this case we have used the NN architecture described in Section 3.2. As before we have built our simulated maps by including CMB and thermal dust, while the low frequency foregrounds may be synchrotron with or without a curved SED and possibly AME.

The training set has been generated from four sets of maps, for a total of more than 1.7×10^9 pixels used for optimizing the NN weights and 3.4×10^8 pixels for validation. The training history is shown in Figure 6: the NN reaches about 87% of accuracy on the training set after 220 epochs, in the noiseless case. It is worth noticing that as a result of the enhanced complexity in the simulations, the NN training takes more time in this case, reaching convergence in about 220 epochs. Results on a test map are shown in Figure 7. In this case the sky is divided into four different regions, corresponding to the four models that the NN has to classify: synchrotron with a pure power law SED (red), synchrotron with

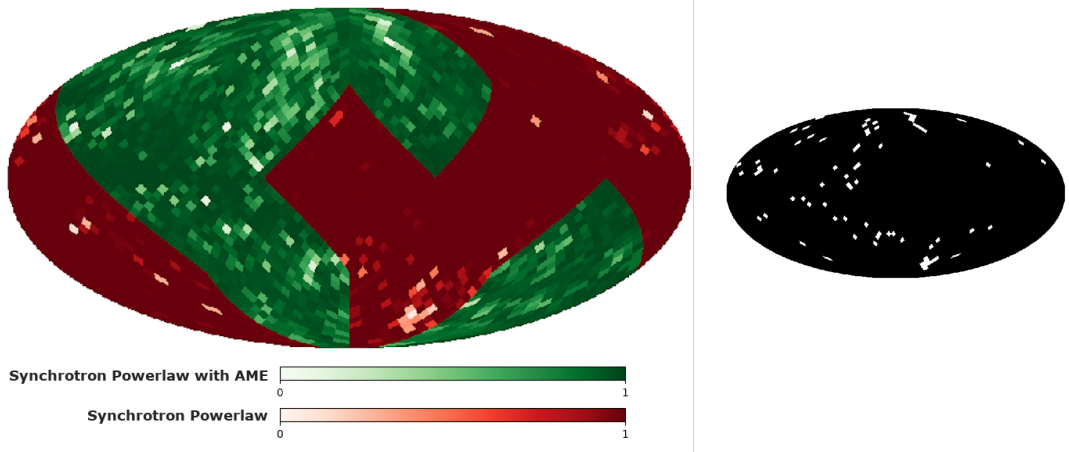


Figure 5. Left panel: NN prediction on test set for the binary classification for power law synchrotron only (red regions) and without AME (green regions). The color bar shows the NN probability assigned to the corresponding and correct synchrotron model across the sky. Right panel: White pixels are those where the wrong model is indicated by the NN with the highest accuracy. These results are for the noiseless case.

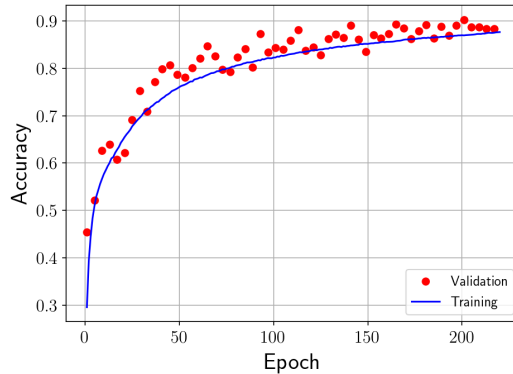


Figure 6. NN accuracy across training with respect to epochs for multi-class classification between synchrotron with and without curvature, with and without AME, in the noiseless case.

running of the spectral index (blue) and possible presence of polarized AME in both cases (green and purple respectively). As before, color bars report the probability assigned by the NN that each pixel corresponds to the correct model, and lighter colors show pixels where the NN have assigned the wrong foreground model. The reached accuracy on the test set is at the level of about 93%.

In Table 2 we report a summary of the performance of the NN in the different considered configurations. We notice that in some cases the accuracy reached on the test set is higher than the one on the training set, this could happen as a consequence of having added used dropout during training.

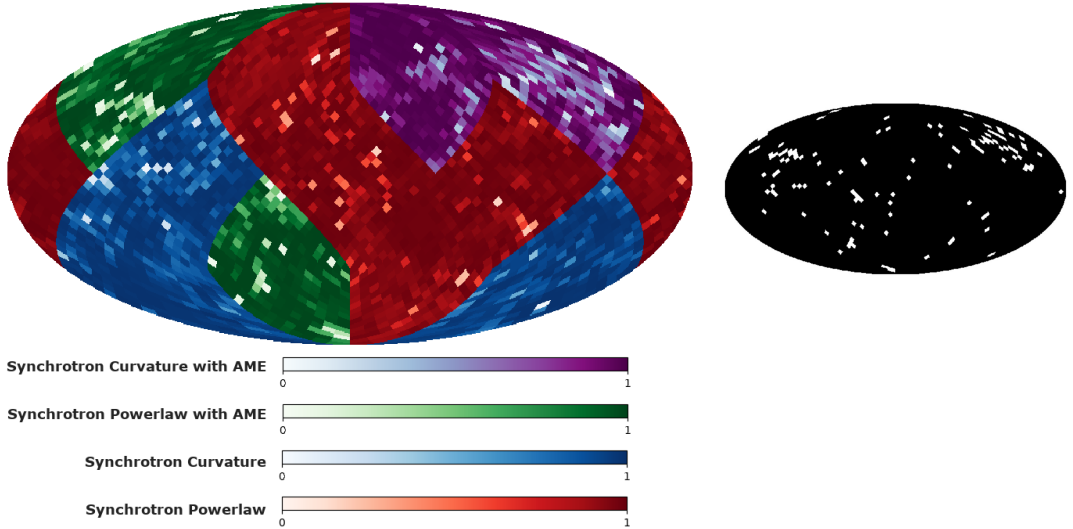


Figure 7. Left panel: NN prediction on test set for the multi-class classification for pure power law synchrotron with (green regions) and without AME (red regions), curvature with (purple) and without (blue) AME. The color bars show the NN probability assigned to the corresponding and correct synchrotron model across the sky. Right panel: white pixels are those where a wrong model is indicated by the NN with the highest accuracy. These results are for the noiseless case.

Sky models	Accuracy on training set	Accuracy on test set
Pure power law & Curvature	99%	98%
AME & Pure power law	93%	97%
AME & Pure power law & Curvature	87%	93%

Table 2. Accuracy on training and test sets of the NN for different sky models in the basic configuration without noise.

4.3 Classification in presence of noise

We have also tested the performances of our NNs in a more realistic case, where instrumental noise is present on maps. In particular, we have considered the specification of the LiteBIRD and QUIJOTE experiments, with the sensitivities reported in Table 1 and uniform noise distribution across the sky.

Our first approach has been to change only the test sets, by adding noise on the test maps, but keeping the weights of the NNs unchanged, therefore with the values optimized with the noiseless training. The first column of Table 3 reports the accuracy reached on the test sets for the three classification problems considered: binary classification for synchrotron models, presence of AME, and multi-classification. For the binary classification, we reached acceptable accuracy; While the accuracy drops significantly, reaching about 68% in the most complex multi-classification case.

To get better results we have trained the NN with noise in the training set. We have considered two different approaches. In the first one, we have added one noise realization on the multi-frequency maps used previously as training set. We have then taken the already trained NN on noiseless data, and performed a second phase of training with the noisy training set. In this way, the NN shows a remarkable increase in accuracy, being able to reach $\sim 90\%$

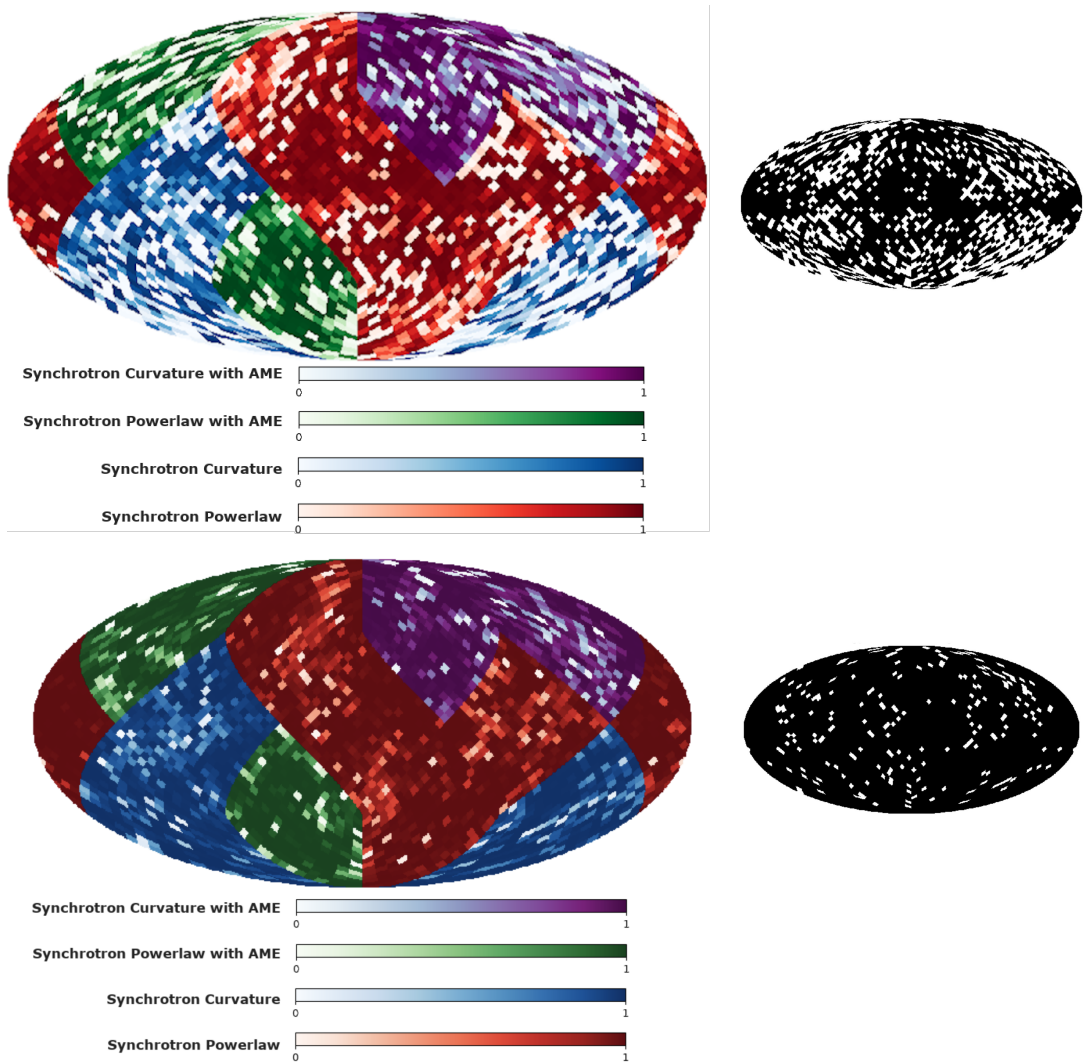


Figure 8. The effect of including the noise in the training set. The color scales for the considered models are the same as Figure 7. The upper panels indicate the NN accuracy on noisy test set and lower panels show the NN accuracy on the same noisy test set after re-training with 100 noise realizations at $N_{side} = 16$; As before, white pixels in the right panels are those where the wrong model is indicated by the NN with the higher probability.

on the test set for the multi-classification. In the second approach, we have built new training sets, consisting in 100 maps of each model at low resolution ($N_{side} = 16$), therefore there are 400 maps which are more than 1 million pixels for the noisy training set. Similarly to the previous case, the reached accuracy is pretty high at the level of about 93%, proving that, during training, the NN is able to learn the noise properties and take those into account during the model classification. In Figure 8 we show the results on the noisy test map for the multi-model classification, for the case in which the training has been done with noiseless simulations (upper panels) and the one where the training set was built from low resolution maps (lower panels). A summary of all the results is reported in Table 3.

Sky models	Acc on test set for training with noiseless data	Acc for Re-Training with $N_{side} = 1024$, 1 noise realization	Acc for Re-Training with $N_{side} = 16$, 100 noise realizations
Pure power law & Curvature	82%	95%	97%
AME & Pure power law	78%	92%	94%
AME & Pure power law & Curvature	68%	90%	93%

Table 3. Accuracy of the NN for the binary and Multi-classification in presence of noise with different approaches for training.

5 Comparison with the χ^2 information

In this Section, we compare quantitatively the information retrieved via our NN apparatus with the ordinary goodness of fit represented by a χ^2 test following a parametric component separation analysis. Here we exploit the approach developed by Stompor et al. [37] which is currently used for quantifying the science outcome of future B -mode probes [4]. We refer to these papers for further details on this approach, limiting ourselves to the definition of quantities of relevance for the present work. The data model is usually written as

$$d_p(\nu) = \sum_c a_p^c(\nu) s_p^c + n_p(\nu) \equiv \mathbf{A}_p s_p + n_p, \quad (5.1)$$

where d_p contains measured signal at each frequency ν and sky direction p , summed over all components whose amplitude is written as s_p^c ; \mathbf{A}_p is the mixing matrix which contains the parametric SED model to fit, depending in principle on the sky direction, and n_p represents the noise. The component separation process consists in obtaining an estimate $\tilde{s}_p = \mathbf{W}_p d_p$ of the components, by means of a kernel operator \mathbf{W}_p , given by

$$\mathbf{W}_p \equiv (\mathbf{A}_p^T \mathbf{N}_p^{-1} \mathbf{A}_p)^{-1} \mathbf{A}_p^T \mathbf{N}_p^{-1}, \quad \mathbf{N}_p \equiv n_p^T n_p, \quad (5.2)$$

where \mathbf{N}_p represents here the noise correlation matrix; the kernel operator is the result of the maximization of the likelihood

$$-2 \log \mathcal{L} = - \sum_p (d_p - \mathbf{A}_p s_p)^T \mathbf{N}_p^{-1} (d_p - \mathbf{A}_p s_p), \quad (5.3)$$

which is valid in the case in which the noise is block diagonal, i.e. correlations are allowed between Stokes parameter in a given pixel only. The χ^2 is defined as

$$\chi^2(p) = \sum_{\nu=1}^{N_{band}} \left(\frac{d_\nu - s_\nu(p)}{\sigma_\nu(p)} \right)^2, \quad (5.4)$$

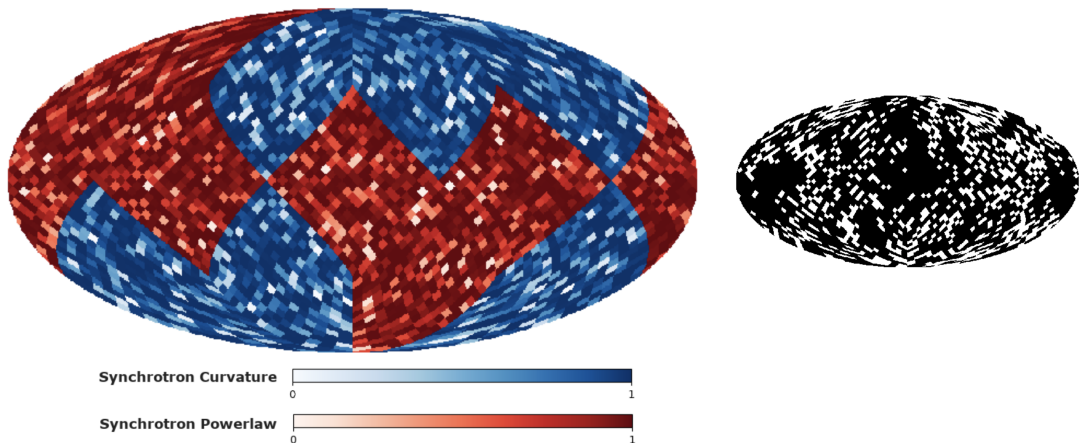


Figure 9. Left panel: Reduced χ^2 probability distribution for pure power law and curvature synchrotron SED, in each pixel of the analysis. Right panel: white pixels indicates disfavour of the right model with respect to the true one via a χ^2 analysis.

Where the $\sigma_\nu(p)$ only corresponds to white noise. The corresponding approach to component separation has been implemented into the publicly available code `ForeGround Buster` `FGBuster`⁴, which we adopt in the rest of the work for calculating the χ^2 after component separation, using the same input maps used so far for the NN. We restrict this analysis to the simplest cases of pure power law and curvature SED for synchrotron, i.e. the first case analyzed in the previous Section, in the binary classification mode. We run `FGBuster` on the corresponding input skies, and calculate the χ^2 accordingly. In one case, the parameters to fit for `FGBuster` are synchrotron, dust amplitudes and synchrotron spectral index, while in the other case, in addition to those, there is synchrotron curvature. Since the parameterization of two synchrotron models are different, to have a fair comparison between two χ^2 we have computed the reduced χ^2 afterwards.

In the left panel of Figure 9 we show the results of reduced χ^2 probability distribution in the two cases, while right panel of Figure 9 shows which model for each pixels is preferred, according to the same distribution, by indicating with white pixels the ones where the χ^2 disfavours the correct model. The corresponding accuracy is therefore about 73%. A comparison of this result with the values reported in Table 3 shows the higher rate of right assignments by the NN. In Figure 10 we also compare the χ^2 values for the two cases across the sky, finding a close correspondence between the sky distribution of differences and the Galactic plane, as expected from a pure χ^2 analysis sensitive to the signal to noise ratio only. The green regions in this figure, far from Galactic plane, refer to the same regions in the right panel of Figure 9 with many white pixels which mislead the χ^2 test. Moreover the reason of low accuracy for discerning two models through χ^2 can be explained by Figure 10, since the χ^2 values for two models in the green regions are so close to each other, any statistical instability in presence of very low signal to noise can deceive to choose the wrong model.

⁴ <https://github.com/fgbuster/fgbuster>

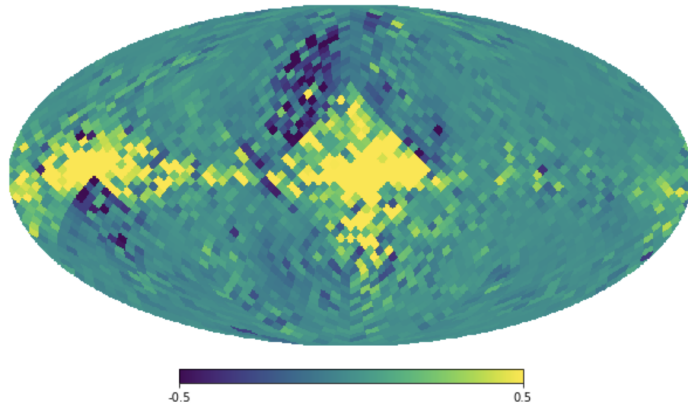


Figure 10. χ^2 difference for pure power law and curvature synchrotron SED. Yellow and dark blue areas prefer pure power law and curvature SED for synchrotron, respectively.

6 Conclusion

With this work we start to investigate the relevance of NN in recognizing the physical properties of the diffuse linearly polarized emission from our own Galaxy at microwave frequencies, which represents the main astrophysical contaminant to the measurement of the CMB B -mode polarization sourced by GWs in the early Universe. The problem is particularly challenging and urgent, due to scientific relevance of the cosmological signal, and the difficulty in disentangle it from the much brighter foreground emission.

Foreground cleaning is usually performed via parametric fitting, which imply the necessity to identifying the physical parameters describing the foreground model in each portion of the sky, fitting and marginalizing them on the basis of a suitable multi-frequency coverage. On the other hand, foreground physical properties and model do vary in the sky, in a manner which is currently only partially revealed by observations, and yet crucial, because the right parametrization of them is necessary to perform a good fitting and prevent the presence of foreground residual in the CMB maps which could bias the scientific results.

In the present work we study the possibility to identify the right physical parametrization of foregrounds, varying across the sky, in a pre-foreground cleaning phase. We do it with NNs, trained on simulations, and applied to test data. We focus on the properties of Galactic synchrotron and AME, which have a rich phenomenology, resulting in possible different parametrization across the sky. We take care of making the simulations substantially different from observations, by explicitly and microscopically altering the training set with respect to the test one, at each resolution element. We find a good performance of the NN in recognize the right parametrization of foregrounds, which achieve better results than a standard χ^2 test on the goodness of fit, making our results interesting and suitable for future studies.

The combination of the simulations based on the specification of the QUIJOTE telescope and the LiteBIRD satellite, with a good coverage of the relevant frequencies, are analyzed in the binary and multi-class classifications modes, i.e. when two and four models have to be recognized in the sky, respectively. In all cases, the rate of success in recognizing the right foreground model is equal or larger than 90%, even in the case where four foreground models have to be recognized, namely pure power law SED with or without curvature for synchrotron, with and without AME. We compare the NN information concerning model recognition with

the χ^2 distribution following a parametric component separation assuming a given model, implemented and run through the publicly available `FGBuster` code. We find that the NN perform better than the χ^2 s, in particular at intermediate and high Galactic latitudes.

We believe that these results are quite interesting, and a promising first step into the construction of a model recognition layer of data analysis in B -mode CMB measurements. Further lines of investigation concern the extension to others foreground models as well as the inclusion of possible realistic systematic effects.

Acknowledgments

The authors thank Luca Heltai and Davide Poletti for useful discussions and suggestions. We acknowledge support from the ASI-COSMOS Network (cosmosnet.it) and by the INDARK INFN Initiative.

References

- [1] W. Hu and M. J. White, *A CMB polarization primer*, *New Astron.* **2** (1997) 323 [[astro-ph/9706147](#)].
- [2] U. Seljak and M. Zaldarriaga, *Signature of gravity waves in polarization of the microwave background*, *Phys. Rev. Lett.* **78** (1997) 2054 [[astro-ph/9609169](#)].
- [3] M. Kamionkowski, A. Kosowsky and A. Stebbins, *Statistics of cosmic microwave background polarization*, *Phys. Rev.* **D55** (1997) 7368 [[astro-ph/9611125](#)].
- [4] P. Campeti, D. Poletti and C. Baccigalupi, *Principal component analysis of the primordial tensor power spectrum*, *JCAP* **1909** (2019) 055 [[1905.08200](#)].
- [5] C. L. Bennett, D. Larson, J. L. Weiland, N. Jarosik, G. Hinshaw, N. Odegard et al., *Nine-year wilkinson microwave anisotropy probe(wmap) observations: Final maps and results*, *The Astrophysical Journal Supplement Series* **208** (2013) 20.
- [6] PLANCK collaboration, *Planck 2015 results. I. Overview of products and scientific results*, *Astron. Astrophys.* **594** (2016) A1 [[1502.01582](#)].
- [7] SPTPOL collaboration, *Detection of B-mode Polarization in the Cosmic Microwave Background with Data from the South Pole Telescope*, *Phys. Rev. Lett.* **111** (2013) 141301 [[1307.5830](#)].
- [8] POLARBEAR collaboration, *A Measurement of the Cosmic Microwave Background B-Mode Polarization Power Spectrum at Sub-Degree Scales from 2 years of POLARBEAR Data*, *Astrophys. J.* **848** (2017) 121 [[1705.02907](#)].
- [9] PLANCK collaboration, *Planck intermediate results. XLI. A map of lensing-induced B-modes*, *Astron. Astrophys.* **596** (2016) A102 [[1512.02882](#)].
- [10] BICEP, KECK collaboration, *Measurements of Degree-Scale B-mode Polarization with the BICEP/Keck Experiments at South Pole*, in *53rd Rencontres de Moriond on Cosmology La Thuile, Italy, March 17-24, 2018*, 2018, [1807.02199](#).
- [11] ACTPOL collaboration, *The Atacama Cosmology Telescope: Two-Season ACTPol Spectra and Parameters*, *JCAP* **1706** (2017) 031 [[1610.02360](#)].
- [12] BICEP2, KECK ARRAY collaboration, *BICEP2 / Keck Array x: Constraints on Primordial Gravitational Waves using Planck, WMAP, and New BICEP2/Keck Observations through the 2015 Season*, *Phys. Rev. Lett.* **121** (2018) 221301 [[1810.05216](#)].
- [13] PLANCK collaboration, *Planck 2018 results. IV. Diffuse component separation*, [1807.06208](#).

- [14] N. Krachmalnicoff, C. Baccigalupi, J. Aumont, M. Bersanelli and A. Mennella, *Characterization of foreground emission on degree angular scales for CMB B-mode observations - Thermal dust and synchrotron signal from Planck and WMAP data*, *Astron. Astrophys.* **588** (2016) A65 [[1511.00532](#)].
- [15] N. Krachmalnicoff et al., *S-PASS view of polarized Galactic synchrotron at 2.3 GHz as a contaminant to CMB observations*, *Astron. Astrophys.* **618** (2018) A166 [[1802.01145](#)].
- [16] POLARBEAR collaboration, *The POLARBEAR-2 and the Simons Array Experiment*, *J. Low. Temp. Phys.* **184** (2016) 805 [[1512.07299](#)].
- [17] SIMONS OBSERVATORY collaboration, *The Simons Observatory: Science goals and forecasts*, *JCAP* **1902** (2019) 056 [[1808.07445](#)].
- [18] CMB-S4 collaboration, *CMB-S4 Science Book, First Edition*, [1610.02743](#).
- [19] A. Suzuki, P. A. R. Ade, Y. Akiba, D. Alonso, K. Arnold, J. Aumont et al., *The litebird satellite mission: Sub-kelvin instrument*, *Journal of Low Temperature Physics* **193** (2018) 1048â$#215;1056.
- [20] S. Ravanbakhsh, J. Oliva, S. Fromenteau, L. C. Price, S. Ho, J. Schneider et al., *Estimating Cosmological Parameters from the Dark Matter Distribution*, [1711.02033](#).
- [21] D. George and E. A. Huerta, *Deep Neural Networks to Enable Real-time Multimessenger Astrophysics*, *Phys. Rev.* **D97** (2018) 044039 [[1701.00008](#)].
- [22] A. Gupta, J. M. Z. Matilla, D. Hsu and Z. Haiman, *Non-Gaussian information from weak lensing data via deep learning*, *Phys. Rev.* **D97** (2018) 103515 [[1802.01212](#)].
- [23] H. U. Norgaard-Nielsen and H. E. Jorgensen, *Foreground removal from CMB temperature maps using an MLP neural network*, *Astrophys. Space Sci.* **318** (2008) 195 [[0809.2914](#)].
- [24] R. Ciuca, O. F. Hernandez and M. Wolman, *A Convolutional Neural Network For Cosmic String Detection in CMB Temperature Maps*, *Mon. Not. Roy. Astron. Soc.* **485** (2019) 1377 [[1708.08878](#)].
- [25] J. Caldeira, W. L. K. Wu, B. Nord, C. Avestruz, S. Trivedi and K. T. Story, *DeepCMB: Lensing Reconstruction of the Cosmic Microwave Background with Deep Neural Networks*, *Astron. Comput.* **28** (2019) 100307 [[1810.01483](#)].
- [26] N. Krachmalnicoff and M. Tomasi, *Convolutional neural networks on the healpix sphere: a pixel-based algorithm and its application to cmb data analysis*, *Astronomy & Astrophysics* **628** (2019) A129.
- [27] J. A. Rubin-Martn, R. Rebolo, M. Aguiar, R. Gnova-Santos, F. Gmez-Reasco, J. M. Herreros et al., *The QUIJOTE-CMB experiment: studying the polarisation of the galactic and cosmological microwave emissions*, in *Ground-based and Airborne Telescopes IV*, L. M. Stepp, R. Gilmozzi and H. J. Hall, eds., vol. 8444, pp. 987 – 997, International Society for Optics and Photonics, SPIE, 2012, [DOI](#).
- [28] C. Dickinson, Y. Ali-Hamoud, A. Barr, E. Battistelli, A. Bell, L. Bernstein et al., *The state-of-play of anomalous microwave emission (ame) research*, *New Astronomy Reviews* **80** (2018) 1â$#215;28.
- [29] B. T. Draine and A. Lazarian, *Electric dipole radiation from spinning dust grains*, *Astrophys. J.* **508** (1998) 157 [[astro-ph/9802239](#)].
- [30] B. T. Draine and A. Lazarian, *Magnetic dipole microwave emission from dust grains*, *Astrophys. J.* **512** (1999) 740 [[astro-ph/9807009](#)].
- [31] R. Gnova-Santos et al., *QUIJOTE scientific results â$#215; I. Measurements of the intensity and polarisation of the anomalous microwave emission in the Perseus molecular complex*, *Mon. Not. Roy. Astron. Soc.* **452** (2015) 4169 [[1501.04491](#)].

- [32] Y. Ali-Haïmoud, C. M. Hirata and C. Dickinson, *A refined model for spinning dust radiation*, *Mon. Not. Roy. Astron. Soc.* **395** (2009) 1055 [0812.2904].
- [33] B. Thorne, J. Dunkley, D. Alonso and S. Næss, *The python sky model: software for simulating the galactic microwave sky*, *Monthly Notices of the Royal Astronomical Society* **469** (2017) 2821–2833.
- [34] A. Kogut, *Synchrotron spectral curvature from 22 mhz to 23 ghz*, *The Astrophysical Journal* **753** (2012) 110.
- [35] J. Errard, S. M. Feeney, H. V. Peiris and A. H. Jaffe, *Robust forecasts on fundamental physics from the foreground-obscured, gravitationally-lensed CMB polarization*, *JCAP* **1603** (2016) 052 [1509.06770].
- [36] I. Goodfellow, Y. Bengio and A. Courville, *Deep Learning*. MIT Press, 2016.
- [37] R. Stompor, S. M. Leach, F. Stivoli and C. Baccigalupi, *Maximum Likelihood algorithm for parametric component separation in CMB experiments*, *Mon. Not. Roy. Astron. Soc.* **392** (2009) 216 [0804.2645].